doi.org/10.54473/IJTRET.2024.8205
International Journal of Trendy Research in Engineering and Technology
Volume 8 Issue 2 April 2024
ISSN NO 2582-0958

SYNTHESIS, CHARACTERIZATION, AND PHOTOCATALYTIC PROPERTIES OF LANTHANIDE-DOPED HEMATITE NANOPARTICLES

Pankaj Kumar
Department of Physics, Career Point University, Hamirpur, Himachal Pradesh 176041, INDIA
*Corresponding Author: pankajkullu22451@gmail.com

Received 18 April 2024 Received in revised form 29 April 2024 Accepted 02 May 2024

ABSTRACT

This work aims to develop a highly efficient UV light-induced photocatalyst based on Sm-doped Hematite (α-Fe_2O_3) nanoparticles (NPs). Sm-doped α-Fe_2O_3 NPs were synthesized via a straightforward co-precipitation technique and subsequently analyzed for their morphological, structural, and functional attributes. Examination under scanning electron microscopy revealed the formation of NPs, often clustered in small aggregates. Transmission electron microscopy measurements indicated a NPs size range of approximately 18 nm. X-ray diffraction analysis confirmed octahedral-shaped with the crystalline nature and geometry of the synthesized NPs, with a determined crystallite size of 13 nm. The photocatalytic efficacy of the Sm-doped α-Fe_2O_3 catalysts was evaluated through their ability to degrade Rhodamine B (RhB) under solar light exposure. Remarkably, Sm-doped α-Fe_2O_3 exhibited outstanding degradation performance, achieving a 96.82% degradation of RhB within 120 minutes under specified conditions ((RhB) = 20 ppm; (catalyst) = 15-25-50 mg/L; pH = 7; T = 30 °C)). The degradation process followed pseudo-first-order kinetics. This exemplary photocatalytic activity suggests that the synthesized NPs hold significant potential for the efficient removal of organic pollutants from industrial wastewater.

Keywords: Hematite nanoparticles; Lanthanide doped; Photocatalytic; X-ray diffraction, SEM,EDX,TEM

INTRODUCTION

The degradation of environmental components has recently emerged as a global crisis, demanding urgent action. Contaminated water presents a significant threat to ecosystem equilibrium, with its quality steadily declining due to the widespread use of chemicals by human activities [1]. Regrettably, despite advancements in science and technology, recent studies have revealed that 11% of the global population lacks access to clean drinking water Industrial effluents often contain non-biodegradable organic pigments that can persist under adverse conditions [2]. These dyes are prone to various physicochemical and photochemical reactions, leading to the formation of numerous secondary compounds that can enter the food chain, causing severe illnesses in humans. Consequently, numerous strategies are under investigation in the quest for effective wastewater management solutions. Various commercially available equipment and techniques exist for removing organic dyes from wastewater [3]. Among these methods, modern photocatalysis stands out due to its distinctive mechanism of action and production of less harmful by-products. During the photocatalytic process, free radical species (such as OH and $O_2^{\bullet}$) are generated on the valence and conduction bands through energy utilization [4]. These unpaired electrons initiate redox reactions in the water, leading to the breakdown of organic dyes into harmless byproducts such as CO_2 and H_2O. Photocatalysts based on lanthanide metal oxides have been utilized for the past three decades. Studied by Fujishima and Honda in the 1990s as a photocatalyst for water purification. α-Fe_2O_3 has emerged as a promising visible-light-driven photocatalyst due to its affordability, abundance, non-toxicity, high stability, and favorable bandgap (Eg = 2.2 eV) [5]. However, its practical use is hindered by its limited total diffusion length (2-4 nm), short excitation lifetime, and restricted light penetration depth. Various strategies have been investigated to improve the suitability of hematite as a photocatalytic material, including nanostructure engineering to improve light absorption, diffusion length, and reaction sites, as well as combining it with other materials such as carbon, metals, and semiconductors to enhance carrier transport [6-7]. Among these approaches, intentional defect engineering has been shown to be a promising technique for improving performance.

Materials with unique physicochemical properties hold great potential for designing efficient photocatalysts. Among the various defects, oxygen vacancies in α-Fe_2O_3 NPs have been investigated extensively, with methods including heat treatment, plasma treatment, ball-milling, and aerosol-assisted chemical vapor deposition [8-11]. Importantly, the synthesis methods significantly influence the generation rate, distribution, role, and behavior of these vacancies. Co-precipitation synthesis stands out as one of the simplest and most cost-effective methods.

Understanding the generation mechanism and behavior of oxygen vacancies in this process is crucial for practical commercialization. In co-precipitation synthesis, FeOOH is initially formed, followed by the transformation to α-Fe_2O_3. The incorporation of lanthanide metals such as La, Ce, Pr, Nd, Gd, Pm, Eu, etc., into α-Fe_2O_3 NPs has been reported to enhance photocatalytic activity [12-15]. For instance, Sm-doped α-Fe_2O_3 NPs synthesized via the co-precipitation method showed improved photocatalytic characteristics, attributed to its higher electron trapping capacity and enhanced oxidation-reduction of organic dyes. Substitution doping of Sm^{2+} at the Fe^{3+} sites in α-Fe_2O_3 NPs has also been explored, leading to alterations in band gap and morphology, thereby improving photocatalytic activity.

In our study, we synthesized Sm-doped α-Fe_2O_3 NPs through thermally induced polymorph transformation. Prior to this, NPs were synthesized using the co-precipitation method. The NPs underwent characterization to assess their structural, optical, and surface chemical properties. Subsequently, their photocatalytic efficiency was evaluated for the decolorization of toxic Rhodamine B (RhB) dye under UV-irradiation.

2. EXPERIMENTAL

2.1 Materials and Synthesis

The synthesis of α-Fe_2O_3 NPs was conducted using the co-precipitation method. Solutions of Ferric chloride hexahydrate ($FeCl_3$•$6H_2O$, 99% purity, Sigma-Aldrich) and Samarium(III) chloride ($SmCl_3.6H_2O$, 99% purity, Sigma-Aldrich) precursors were prepared separately in water at room temperature, with a molar ratio of 1:2, respectively. These precursor solutions were then mixed under continuous magnetic stirring. After 1 hours of stirring, 1M solution of Polyvinylpyrrolidone (PVP) precipitating agent and NaOH was added dropwise while monitoring the pH of the solution. Stirring was halted when the solution reached a pH of approximately 11, and the mixture was allowed to settle undisturbed for 15 minutes. This process resulted in the formation of black precipitates, which were collected by filtration and washed thoroughly with distilled water and ethanol. The black precipitates were then dried in an oven at 80 °C for 12 hours to obtain α-Fe_2O_3 NPs.

2.2 Characterization

The pure and Zr-doped α-Fe_2O_3 NPs underwent characterization using various techniques. X-ray diffraction (XRD) analysis of the powder samples was performed using a Bruker X-ray diffractometer with Cu Kα (λ=1.54 Å) monochromatic wavelength. Vibrational spectroscopy was conducted using a Fourier-transform infrared (FTIR) instrument from Perkin Elmer. Powder samples were prepared into pallets with KBr, and spectra were recorded in the wavenumber range of 4000 to 400 cm-1 in transmission mode. Surface morphology and particle size were examined using a field emission scanning electron microscope (FE-SEM), specifically the ZEISS Supra 55 VP model. Additionally, transmission electron microscopy (TEM) analysis was carried out using a JEOL 1010 instrument from Tokyo, Japan.

2.3 Measurement of Photocatalytic activity

A study employing photocatalysis was conducted in a custom-built reactor equipped with a magnetic stirrer and a UV lamp. The photocatalytic activities of synthesized Sm-doped α-Fe_2O_3 NPs were investigated for the degradation of (RhB) dye solution under illumination from a 125 W (UV-C, 254 nm) Mercury lamp (Phillips). In the experimental setup, different concentrations (15-25-50 mg) of the photocatalyst were added to 100 ml of a 20 ppm dye solution. At regular intervals of 12 minutes, approximately 6 ml of the irradiated solutions were extracted, and the absorption spectra of the solutions were analyzed to monitor the photocatalytic activity.

3. RESULTS AND DISCUSSION

3.1. Structural analysis

X-ray powder diffraction was employed to examine the structure and phase stability of Sm-doped α-Fe_2O_3 NPs. The powder samples revealed a crystalline structure, as depicted in Fig. 1. Based on the JCPDS Card No. 33–0664 [17], all observed peaks could be indexed in accordance with the predicted rhombohedral (hexagonal) structure of doped α-Fe_2O_3 NPs (space group: R-3c) with specific lattice parameters. The diffracting peaks of all prepared samples were evident within the 2θ range, with corresponding miller indices such as (012), (220), (104), (113), (111), (024), (116), (018), (214), and (300) respectively. The uniform intensities observed across the peaks can be attributed to the consistent annealing temperature used during sample preparation, which directly influences the sample's crystallinity and charge mobility. No observable peak shifts were noted across the XRD patterns, consistent with previous findings [18]. This observation suggests that the dopants had no significant impact on the structure of the α-Fe_2O_3 NPs.

The crystallite size (D) was determined using the Debye-Scherrer formula as shown in Equation 1.

$$D = \frac{k\lambda}{\beta \cos\theta} \quad (1)$$

The Debye-Scherrer formula utilizes a factor (K = 0.9), representing the Scherrer constant, alongside the wavelength (λ) of Cu Kα, the Full Width at Half Maximum (FWHM) denoted by β, and the diffracting angle (θ).

The analysis of XRD data revealed an average crystallite size (D) of 13.44 nm, interplanar spacing (d) of 2.6223, lattice parameters (a=b) of 5.012, lattice parameter (c) of 13.71, volume (V) of 292.89, dislocation density (δ) of 0.00630, strain (ε) of 0.00949, stress (σ) of 0.04120, and crystallinity of 94.419%. This indicates that the size of Sm-doped α-Fe_2O_3 NPs decreases due to an increase in nucleation center density in the doped samples. This finding aligns with previous research on Pt-Ru doped hematite NPs [19]. Studies conducted by further support this observation, suggesting that the decrease in crystallite sizes with an increase in dopant concentration results from enhanced nucleation of particles in the host sample [20].

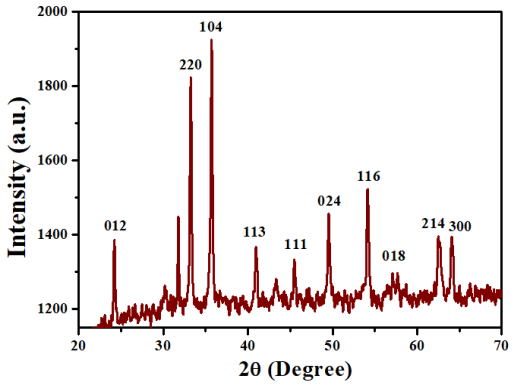

Fig. 1. XRD pattern of hematite crystal lattices of Sm-doped α-Fe_2O_3 NPs

3.2. Functional Group Analysis

FTIR analysis was conducted to determine the likely presence of reducing and stabilizing biomaterials in the fungal biomass extract. The resulting FTIR spectrum displayed several absorption bands that aligned with the functional groups of the Sm-doped α-Fe_2O_3 NPs, as illustrated in Figure 2. Various absorption peaks were observed, including those centered at 3425, 2928, 2429, 1620, 1384, 1076, 461, and 594 cm−1, which were attributed to O–H stretching vibrations, C=O stretching vibrations, C–O stretching vibrations, and the bending vibration of C-OH. The peak at 2928 cm^{-1} indicated the C-H asymmetric and symmetric stretching vibrations of the methyl group [21]. Additionally, a peak at 1635 cm^{-1} could be attributed to the C=O stretching vibration band of polyphenol chemicals present in the PVP, which acted as a stabilizing and capping agent. Bands observed at 918-1110 and 1383 cm^{-1} were associated with the stretching vibration of C-O and polyphenol compounds, along with in-plane bending vibrations of OH in phenols. Furthermore, peaks at 459 and 582 cm^{-1} corresponded to Fe-O stretching vibrations. Peaks in the 500-1000 cm^{-1} wavelength range mainly originated from metal–oxygen group bonding [22], confirming the production of α-Fe_2O_3 NPs.

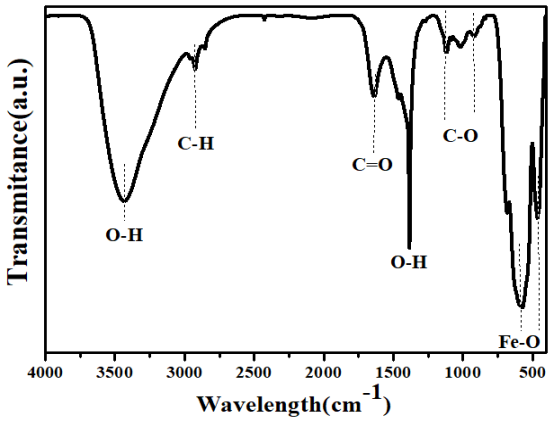

Fig. 2. FTIR spectrum of the developed synthesized Sm-doped α-Fe_2O_3 NPs

3.3. Morphology Analysis

SEM and EDX analyses were conducted to assess the morphology and chemical composition of the Sm-doped α-Fe_2O_3 NPs. In Figure 3a, fine grains with irregular shapes and some agglomeration were observed, indicating the presence of α-Fe_2O_3 NPs. Figure 3b displays the EDX spectrum of α-Fe_2O_3 NPs, detecting peaks corresponding to Fe and O elements, confirming the high purity of the synthesized NPs [23]. Furthermore, TEM investigation was employed to examine the morphology and size of the Sm-doped α-Fe_2O_3 NPs. TEM micrographs revealed octahedral-shaped particles evenly distributed without significant aggregation (Figure 4a). The Histogram image demonstrated well-dispersed particles, with an average diameter of approximately 18.32 nm, determined using ImageJ software (Figure 4b). These findings are consistent with previous studies. For instance, research by synthesize spherical α-Fe_2O_3 NPs with an average size of 70 nm [24]. Additionally, spherical α-Fe_2O_3 NPs ranging in size from 20 to 80 nm have been effectively manufactured using a similar approach [25].

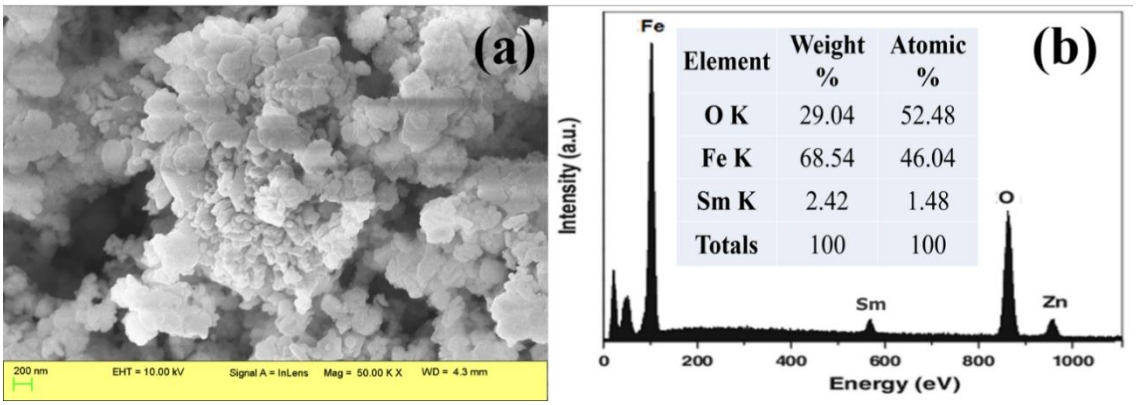

Fig. 3. (a) SEM and (b) EDX images of crystal lattices of Sm-doped α-Fe_2O_3 NPs.

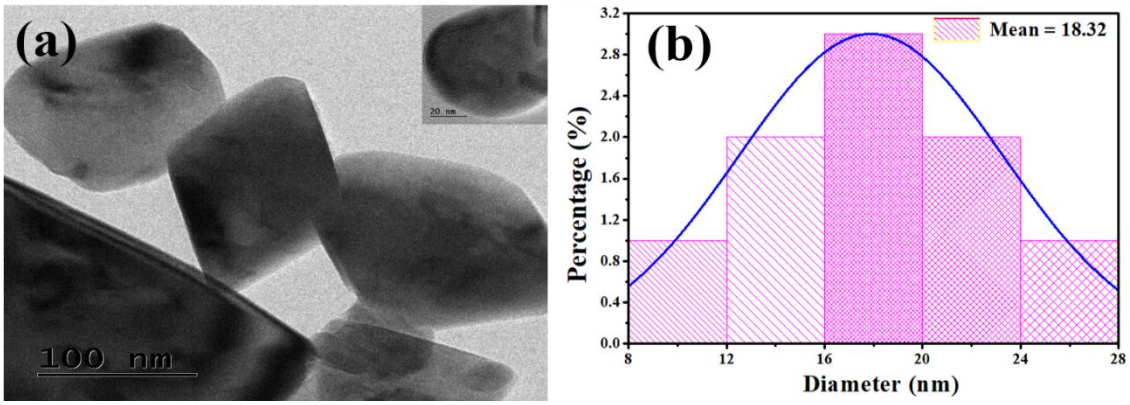

Fig. 4. (a) TEM and (b) Histogram images of crystal lattices of Sm-doped α-Fe_2O_3 NPs.

3.4. Photocatalytic Activity Study

The photocatalytic activity of the α-Fe_2O_3 NPs for degrading methylene blue dye under sunlight irradiation was assessed. The degradation of RhB dye under UV-light irradiation was also observed. In the presence of the catalyst, the intensity of the peak at 550 nm decreased, and complete degradation was observed after 120 minutes. Figure 5 illustrates the photocatalytic activity. The photodegradation efficiency of the Sm-doped α-Fe_2O_3 NPs, as depicted in Figure 5a, indicates that 96% of the dye decomposed after 120 minutes of irradiation. Equation 2 was utilized to calculate the dye degradation percentage (%):

$$(\%\ degradation) = \frac{Co-Ct}{Co} \times 100 \quad (2)$$

Co represents the initial absorption of the solution, while Ct represents the final absorption of the solution. The photodegradation reaction data can be described well by pseudo-first-order reaction kinetics, given by Equation 3, and Shown in Figure 5b.

$$\ln \frac{Co}{C} = \kappa t \quad (3)$$

The pseudo-first-order reaction rate constant (k) is determined by the concentrations (Co and C) at the beginning and at a specific time, respectively, with t representing the radiation exposure time. Table 1 outlines the calculated percentage degradation, rate constant, and regression coefficient for doped α-Fe_2O_3 NPs. Doped α-Fe_2O_3 NPs based nanoplatforms exhibit robust photocatalytic capabilities, along with non-toxicity, biocompatibility, and cost-effectiveness, suggesting their potential to replace traditional dye remediation techniques [26]. Nanoplatforms designed for wastewater treatment, emphasizing photocatalytic properties and environmentally friendly chemistry, are essential. Their exceptional chemical and thermal reliability, ability to absorb visible light, non-toxicity, abundance, and environmental friendliness render them valuable as photocatalysts for pollutant degradation [27].

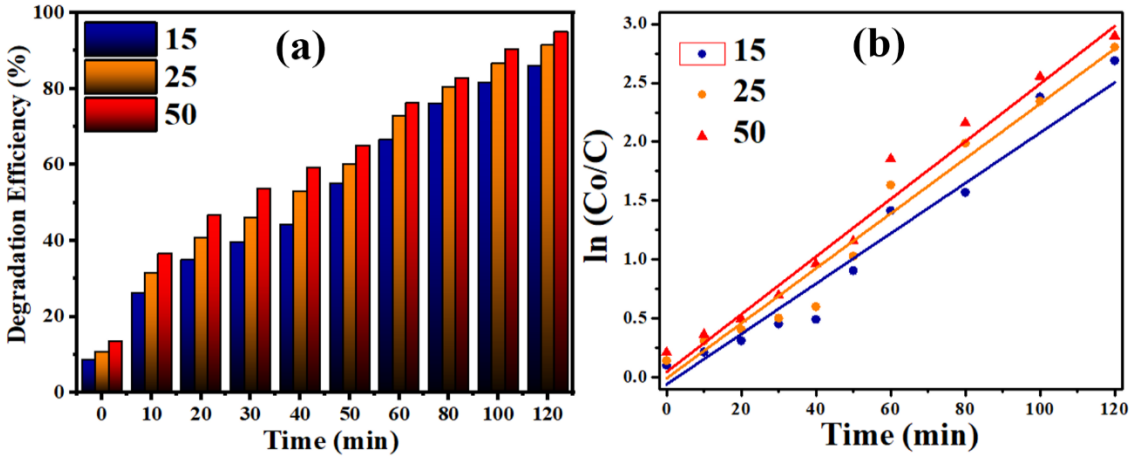

Fig. 5. (a) Degradation percentage and (b) Photodegradation kinetics of synthesized doped α Fe2O3 NPs for RhB dye

Table 1. % degradation, rate constant, and regression coefficient of synthesized Sm-doped α Fe_2O_3 NPs for RhB dye

Method of Synthesis	Concentrations (mg)	Degradation (%)	Rate constant (min^{-1})	Regression coefficient (R^2)
doped α Fe_2O_3 NPs	15	90	0.0079	0.93043
	25	92	0.0085	0.96965
	50	96	0.0091	0.98523

When electrons in Sm-doped α-Fe_2O_3 are excited to move from the valence band to the conduction band when UV light equal to or higher than its band gap energy is absorbed. In the conduction band, this action releases free electrons and leaves holes in the valence band. Water and oxygen molecules stick to the catalyst's surface, α-Fe_2O_3 NPs. The valence band's positive holes then start the oxidation of OH^- ions or water molecules at the catalyst surface, which produces strong oxidizing agents called •OH radicals [28]. Following their reaction with RhB dye, these hydroxyl radicals produce CO_2 and H_2O [29]. At the same time, molecular oxygen adsorbed onto the catalyst surface quickly absorbs the electrons that are already there where they undergo reduction to produce anions of superoxide radical ($O_2^{\bullet-}$). The superoxide radical anion's oxidation potential enables it to react with the RhB dye, producing CO_2 and H_2O in the process [30]. Moreover, the findings from scavenging experiments highlight the crucial involvement of reactive oxygen species (ROS) in the photocatalytic breakdown of organic pollutants. This suggests that doping Sm not only enhances the inhibition of carrier charge recombination but also provides an additional active site response.

4. CONCLUSION

In this study, Sm-doped α-Fe_2O_3 NPs were effectively biosynthesized. Various analytical techniques including FTIR spectroscopy, XRD, SEM, and TEM were employed to characterize the synthesized Sm-doped α-Fe_2O_3 NPs. The doped α-Fe_2O_3 NPs exhibited spherical morphology for the α-Fe_2O_3 phases and rhombohedral crystal lattices, with crystallite sizes measured at 13.44 nm, confirming their existence and crystallinity via XRD analysis. FTIR spectra analysis identified the active molecules responsible for the inhibition and stabilization of the NPs, with characteristic peaks of the Fe-O bonding observed at 459 and 582 cm^{-1}. The energy dispersive X-ray spectroscopy (EDX) spectrum confirmed the presence of oxygen, samarium, and iron in the synthesized material. TEM imaging further confirmed the octahedral form of the Sm-doped α-Fe_2O_3 NPs, with a size range of 18.32 nm. These doped α-Fe_2O_3 NPs exhibit promising photocatalytic activity for degrading dyes in wastewater treatment, owing to their facile synthesis in large quantities using readily available iron precursors. Industries may benefit from large-scale production of NPs using green techniques for dye removal from various wastewaters. Moreover, the synthesized α-Fe_2O_3 NPs demonstrated high photocatalytic effectiveness, degrading 96.82% of Rhodamine B (RhB) dyes under 120 minutes of light exposure. These findings underscore the high potential of Sm-doped α-Fe_2O_3 NPs for dye degradation, suggesting their future application in mitigating hazardous dyes in contaminated water. Additionally, the production process of NPs is rapid, cost-effective, and environmentally benign.

ACKNOWLEDGMENTS

The authors are thankful to the SAIF Panjab University, and Sprint Testing Solutions, Mumbai for assistance in characterizing the synthesized samples.

CONFLICT OF INTEREST

The authors declare no competing financial interest.

REFERENCES

1. Devendrapandi, G., Liu, X., Balu, R., Ayyamperumal, R., Arasu, M.V., Lavanya, M., Reddy, V.R.M., Kim, W.K. and Karthika, P.C., 2024. Innovative remediation strategies for persistent organic pollutants in soil and water: A comprehensive review. Environmental Research, p.118404.

2. Ali, Q.A., 2024. Proposed Solutions to Improve Deterioration of Drinking Water Quality. Global Scientific Review, 23, pp.34-46.

3. Gomaa, H.E., Gomaa, F.A. and Alotaibi, A.A., 2024. Simple, Low-Priced, of Single-Step, and Fast Method for Fabricating and Immobilizing a Commercially Viable Catalyst for the Removal of Azo-Dyes from Water. Arabian Journal for Science and Engineering, 49(1), pp.577-598.

4. Zhang, X., Li, X., Yu, P., Yu, Y., Fan, X., Zhang, J., Yu, Y., Zheng, H. and Sun, Y., 2023. Photocatalytic O2 activation by metal-free carbon nitride nanotube for rapid reactive species generation and organic contaminants degradation. Journal of Hazardous Materials, 456, p.131715.

5. Wan, H., Hu, L., Liu, X., Zhang, Y., Chen, G., Zhang, N. and Ma, R., 2023. Advanced hematite nanomaterials for newly emerging applications. Chemical Science, 14(11), pp.2776-2798.

6. Zhang, X. and Yang, P., 2023. Role of graphitic carbon in g-C3N4 nanoarchitectonics towards efficient photocatalytic reaction kinetics: A review. Carbon, p.118584.

7. Ahmed, S.F., Kumar, P.S., Ahmed, B., Mehnaz, T., Shafiullah, G.M., Duong, X.Q., Mofijur, M., Badruddin, I.A. and Kamangar, S., 2024. Carbon-based nanomaterials: Characteristics, dimensions, advances and challenges in enhancing photocatalytic hydrogen production. International journal of hydrogen energy, 52, pp.424-442.

8. Suardana, P., Sumadiyasa, M., Sudatri, N.W., Suharta, W.G. and Ngurah Gunawan, A.A., 2024. Synthesis of Hematite Crystals from Natural Iron Sand: The Influence of Heating on Optical and Magnetic Properties. Journal of Composite & Advanced Materials/Revue des Composites et des Matériaux Avancés, 34(1).

9. Bootluck, W., Khongnakorn, W., Jutaporn, P., Luengchavanon, M. and Limbut, W., 2023. Enhancement of S-scheme heterojunction hematite and titanium dioxide nanocomposite by plasma treatment in the photocatalytic membrane for hydrogen separation. Journal of Environmental Chemical Engineering, 11(5), p.110674.

10. Fathi, A., Ahmadi, M., Madrakian, T., Afkhami, A. and Asadi, S., 2023. A multi-nebulizer-based aerosol-assisted system for the synthesis of magnetic iron mixed metal oxides nanoparticles (MFe2O4, M= Fe2+, Ni2+, Mn2+, Co2+, Zn2+). Chemical Papers, 77(11), pp.6933-6946.

11. Catto, A.C., Bernardini, S., Aguir, K., Longo, E. and da Silva, L.F., 2023. In-situ hydrothermal synthesis of oriented hematite nanorods for sub-ppm level detection of ozone gas. Journal of Alloys and Compounds, 947, p.169444.

12. Abdallah, A.M., Rabaa, M., Basma, H., Bitar, Z., Yaacoub, N., Sayed Hassan, R. and Awad, R., 2024. Enhancement of the physico-mechanical properties of La-doped Mg–Ni–Co tri-ferrites. Journal of Materials Science: Materials in Electronics, 35(3), p.245.

13. Korkmaz, A.D., 2023. Intrinsic magnetic-optical features of Dy3+ ion substituted NiCuZn nanospinel ferrites via sonochemical approach. Physica B: Condensed Matter, 654, p.414741.

14. Kumar, V., Ahlawat, D.S., Singh, A. and RadheShyam, 2023. Effect of La3+ doping concentration on the structural, electrical, dielectric, and magnetic properties of α-Fe2O3 nanoparticles. Journal of Materials Science: Materials in Electronics, 34(28), p.1947.

15. Sharma, I. and Kumar, P., 2021. Synthesis and Characterization of Mn-Zn soft ferrite nanoparticle of [Gd. sup. 3+] doped. European Journal of Molecular and Clinical Medicine, 8(4), pp.1-10.

16. Aalim, M. and Shah, M.A., 2023. Role of oxygen vacancies and porosity in enhancing the electrochemical properties of Microwave synthesized hematite (α-Fe2O3) nanostructures for supercapacitor application. Vacuum, 210, p.111903.

17. Aalim, M. and Shah, M.A., 2023. Role of oxygen vacancies and porosity in enhancing the electrochemical properties of Microwave synthesized hematite (α-Fe2O3) nanostructures for supercapacitor application. Vacuum, 210, p.111903.

18. Zabara, M.A., Ölmez, B., Alkan Gürsel, S. and Yürüm, A., 2023. Morphology-dependent investigation of Li-ion insertion into single crystal hematite α-Fe2O3 nanostructures. The Journal of Physical Chemistry C, 127(42), pp.20608-20619.

19. Petrović, Ž., Ristić, M., Kraljić Roković, M., Zadro, K., Kuzmann, E., Homonnay, Z., Musić, S. and Krehula, S., 2023. Effects of Pt and Ru doping on the magnetic, optical, photoelectrochemical and photocatalytic properties of electrospun hematite (α-Fe2O3) fibres. Journal of materials research, 38(4), pp.974-989.

20. Irshad, I., Lone, A.G. and Want, B., 2024. Exploring the magnetic, optical and dielectric

properties of Cr-doped hematite (α-Fe (2− x) CrxO3): A comprehensive study. Journal of Alloys and Compounds, 971, p.172696.
21. Haddad, B., Pandey, D.K., Singh, D.K., Paolone, A., Drai, M., Villemin, D. and Bresson, S., 2023. Effect of isopropyl side chain branching and different anions on electronic structure, vibrational spectra, and hydrogen bonding of isopropyl-imidazolium-based ionic liquids: Experimental and theoretical investigations. Spectrochimica Acta Part A: Molecular and Biomolecular Spectroscopy, 291, p.122325.
22. Campanale, C., Savino, I., Massarelli, C. and Uricchio, V.F., 2023. Fourier transform infrared spectroscopy to assess the degree of alteration of artificially aged and environmentally weathered microplastics. Polymers, 15(4), p.911.
23. Sreedhara, R., Krushna, B.R., Sharma, S.C., Nadar, N.R., Krithika, C., Joy, F.D., Shivakumar, V., Devaraja, S., Manjunatha, K., Hsu, T.E. and Wu, S.Y., 2024. Straightforward green synthesis of Fe3+ doped ZnAl2O4 spinel structure and potential applications in alleviating thrombosis, oxidative stress, data encryption and dermatoglyphics. Surfaces and Interfaces, 46, p.104005.
24. Ayub, M., Bashir, M., Majid, F., Shahid, R., Khan, B.S., Saeed, A., Shaik, M.R., Kuniyil, M., Shaik, B. and Khan, M., 2023. Eggshell-Mediated Hematite Nanoparticles: Synthesis and Their Biomedical, Mineralization, and Biodegradation Applications. Crystals, 13(12), p.1699.
25. Jayaseelan, S.J., Parasuraman, K., Anburaj, D.B., Jothibas, M. and Arunkumar, B., 2023. The impacts of Mn ion incorporation on the structural, optical, and magnetic properties of hematite NPs. Nanotechnology for Environmental Engineering, 8(1), pp.15-26.
26. Mersal, M., Zedan, A.F., Mohamed, G.G. and Hassan, G.K., 2023. Fabrication of nitrogen doped TiO2/Fe2O3 nanostructures for photocatalytic oxidation of methanol based wastewater. Scientific Reports, 13(1), p.4431.
27. Ashraf, A., Wahab, R., Al-Khedhairy, A.A., Khan, A. and Rahman, F., 2024. Magnetically separable and visible light-driven photocatalytic activity of graphene oxide based α-Fe2O3 nanocomposite. Materials Chemistry and Physics, p.129111.
28. Li, X., Su, Z., Jiang, H., Liu, J., Zheng, L., Zheng, H., Wu, S. and Shi, X., 2024. Band Structure Tuning via Pt Single Atom Induced Rapid Hydroxyl Radical Generation toward Efficient Photocatalytic Reforming of Lignocellulose into H2. Small, p.2400617.
29. Alsulmi, A., Mohammed, N.N., Soltan, A., Messih, M.A. and Ahmed, M.A., 2023. Engineering S-scheme CuO/ZnO heterojunctions sonochemically for eradicating RhB dye from wastewater under solar radiation. RSC advances, 13(19), pp.13269-13281.
30. Ramanathan, S., Kasemchainan, J., Chuang, H.C., Sobral, A.J. and Poompradub, S., 2023. Rhodamine B dye degradation using used face masks-derived carbon coupled with peroxymonosulfate. Environmental Pollution, 324, p.121386.